



# 1 Performance evaluation of a Semivolatile Aerosol Dichotomous 2 Sampler (SADS) for Exposure Assessment: impact of design 3 issues.

4 Noredine Rekeb<sup>1,2</sup>, Benjamin Sutter<sup>1</sup>, Emmanuel Belut<sup>1</sup>, Evelyne Géhin<sup>2</sup>, Raymond Olsen<sup>3</sup>

5 <sup>1</sup>INRS, National institute for research and safety, Rue du Morvan, 54519, Vandoeuvre-lès-Nancy, France

6 <sup>2</sup>Univ Paris Est Creteil, CERTES, F-94000 Creteil, France

7 <sup>3</sup>STAMI, National Institute of Occupational Health, Pb 5330 Majorstuen, N-0304 Oslo, Norway

8

9 *Correspondence to:* Benjamin Sutter (benjamin.sutter@inrs.fr)

10 **Abstract.** Aerosols of semivolatile organic compounds (SVOCs) pose significant health risks to workers in various  
11 occupational settings. Measuring human exposure to these aerosols requires a separate assessment of the  
12 contribution of particles and gases, which is not resolved by existing sampling techniques. Here, we investigate  
13 experimentally the performance of the Semivolatile Aerosol Dichotomous Sampler (SADS), proposed in previous  
14 studies, for sampling monodisperse liquid particles with aerodynamic diameters between 0.15 and 4.5  $\mu\text{m}$ ,  
15 corresponding to workplace aerosols. The measured sampling performances are compared to their theoretical  
16 counterparts computed by computational fluid dynamics. The effects of leakage rate, repeatability of the assembly,  
17 imprecision of the actually machined nozzle diameters and SADS parts misalignment are examined. The SADS  
18 assembly is found easily leaky, but consequences on sampling can be overcome when a prior leak test with leakage  
19 rate below 4  $\text{Pa}\cdot\text{s}^{-1}$  is passed. Variation of nozzle diameters in the range (-4.5 %, +3.7 %) with respect to nominal  
20 values affects marginally (<3 %) aerosol transmission efficiency, but sampling performance is little reproducible  
21 during successive SADS assemblies (CV=22.1 % for wall losses). Theoretically unpredicted large (40-46 %) wall  
22 losses are measured for particles larger than 2  $\mu\text{m}$ , located mostly (80 %) on the external walls of the collection  
23 nozzle. Assembly repeatability issues and simulations of SADS parts misalignment effect by CFD suggest that  
24 these undesirable particle deposits are due to the mechanical backlashes of the assembly. Thus, the current design  
25 does not guarantee a nozzle misalignment of less than 5 % of the acceleration nozzle diameter, and other important  
26 geometric parameters are not further constrained. The promising theoretical sampling performance of the SADS  
27 for SVOCs aerosol larger than 1  $\mu\text{m}$  thus falls short of expectations due to mechanical design issues that can be  
28 improved before possible field use.

## 29 1 Introduction

30 Semivolatile organic compounds (SVOCs) represent a significant subgroup of volatile organic compounds  
31 (VOCs), and their presence in the environment raises concerns due to their association with carcinogenic,  
32 mutagenic, and reprotoxic effects (Raffy et al., 2018). One of the defining features of SVOCs is their ability to  
33 exist simultaneously in both vapour and particle phases, making their sampling and analysis a complex task. There  
34 are varying definitions of SVOCs, with the U.S. Environmental Protection Agency (Technical Overview of  
35 Volatile Organic Compounds, 2020) proposing a classification based on boiling points (240-380 °C at atmospheric



36 pressure), while the standard EN 13936 defines them according to their saturation vapour pressure (ranging from  
37 0.001 to 100 Pa at room temperature).

38 In occupational settings, SVOCs can be encountered in diverse forms, such as metalworking fluid (MWF) mists,  
39 phthalates, pesticides, acrylamides, machining fluids, exhaust gases from diesel engines, and more. Exposure to  
40 these pollutants in the workplace can pose health risks to workers, depending on their chemical nature and the  
41 extent of exposure. Understanding the health implications requires accurate measurement of both vapour and  
42 particle phases, as their behaviour and effects can differ when inhaled in the respiratory system. Notably, the  
43 vapour phase's absorption in the respiratory tract is influenced by the SVOC's solubility, while particle deposition  
44 in the lung is governed by their aerodynamic diameter (Volckens, 2003). Additionally, direct adsorption of SVOCs  
45 on the skin can lead to absorption into the body (Roberts et al., 2009). Thus, it becomes essential to separately  
46 quantify the concentrations of each phase that constitutes a semivolatile aerosol.

47 Various sampling techniques have been proposed to evaluate semivolatile aerosol concentrations, including  
48 filtration methods, thermodesorption tubes, cyclones, electrostatic precipitators, and multiple "filter + adsorbent"  
49 devices. However, these methods often suffer from the issue of evaporation of the particulate phase during  
50 sampling, leading to biased measurements. Filtration methods, for instance, have been found to underestimate  
51 particle concentrations due to continued evaporation from the filter during sampling (Park et al., 2015; Raynor et  
52 al., 2000; Simpson, 2003; Simpson et al., 2000; Volckens et al., 2010). Other techniques that do not instantaneously  
53 separate particles and vapour also face the problem of evaporation during sampling (Raynor and Leith, 1999; Leith  
54 et al., 2010; Lillienberg et al., 2008; Wlaschitz and Höflinger, 2007; Sutter et al., 2010; Kim and Raynor, 2010a).  
55 As of now, no applicable model exists to theoretically calculate the evaporation of a semivolatile aerosol during  
56 workplace air sampling, which hampers the use of these techniques.

57 An alternative approach is the Virtual Impactor (VI) principle, inspired by classical inertial impactors with  
58 collection plates (Loo and Cork, 1988; Marple and Chien, 1980). The VI is employed for size classification of  
59 particles based on their aerodynamic diameter. In 2009, the Semivolatile Aerosol Dichotomous Sampler (SADS),  
60 a novel variant of the VI dedicated to SVOCs, was proposed by Kim and Raynor (2009) and raised great hopes  
61 for this application.

62 In its original version, the SADS features an inverted flow configuration between the major and minor flows,  
63 resulting in 86 % of the total air being directed into the collection nozzle, while the remaining 14 % is suctioned  
64 perpendicular to the acceleration nozzle axis (Figure 1). The aerosol is sampled through a 4 mm inlet orifice and  
65 accelerated through a convergent shape called the "acceleration nozzle", which narrows to a 0.8 mm orifice  
66 diameter. In the separation space, inertial particles are directed into the collection nozzle, while non-inertial  
67 particles and vapours follow both the major and minor flows. The collection nozzle, located 1.2 mm from the  
68 acceleration nozzle, has a diameter of 1.1 mm, and filters and adsorbent beds are placed at each outlet (major and  
69 minor flow). The SADS operates at a total sampling flow rate of 2.1 L.min<sup>-1</sup>, split into 1.8 L.min<sup>-1</sup> at the major  
70 flow outlet and 0.3 L.min<sup>-1</sup> at the minor flow outlet (split ratio of 0.143).

71 The SADS was further optimized numerically and tested both in the laboratory and in the field by its designers  
72 (Kim and Raynor, 2010a, b; Kim et al., 2014). The optimized version is characterized essentially by a revised split  
73 ratio of 0.1 with a total sampling flow rate of 2 L.min<sup>-1</sup> and with a length of the separation space reduced to  
74 0.48 mm instead of 1.2 mm. The angle of the acceleration nozzle was also changed from 19° to 45° between the  
75 2009 and 2010 versions. Despite these modifications, the overall mechanical design of the SADS has not changed



76 between these two versions (Figure 3). The overall shape of the device is that of a 37 mm cassette, and it is made  
77 up of two parts that fit together via a cylindrical bearing surface. The parts are held together by 2 screws. Sealing  
78 is ensured by an O-ring between the two parts, pressed together by the two screws.  
79 Thus, the work of Kim et al. led to the creation of the SADS concept and revealed its interest in the sampling of  
80 semi-volatile aerosols. However, many questions remain before SADS can be considered sufficiently mature for  
81 widespread use as a portable sampling device for SVOC aerosols.  
82 Firstly, the sampling performance of the device was not evaluated in detail for particles with aerodynamic  
83 diameters greater than 1  $\mu\text{m}$ , as the initial device was not designed for this. However, for field use, the evaluation  
84 of the performance of the SADS for particles above 1  $\mu\text{m}$  is especially important because workplace SVOCs  
85 aerosols showed a presence of particles with diameters up to 10  $\mu\text{m}$  (Cooper et al., 1996; Park et al., 2009). Since  
86 the metric of SVOC exposure is mass concentration, and the mass carried by particles increases with the cube of  
87 their diameter, sampling errors on the most inertial particles generate biases in exposure measurements that are far  
88 more problematic than sampling errors on sub-micron particles. Optimization work by Kim et al. focused on  
89 reducing the cut-off diameter of the device around an aerodynamic diameter of 0.7  $\mu\text{m}$ , but the impact on super-  
90 micron particle sampling was not assessed. Subsequent tests on real aerosols revealed significant deposits in the  
91 device that had not been anticipated by the theoretical study, and the exact origin of these deposits is still unknown  
92 (26.5 % of wall losses for an aerosol with MMAD of 2.17  $\mu\text{m}$  in Kim and Raynor (2010b) and separate evaluations  
93 by NIOH, Norway and Fraunhofer ITEM showed similarly high deposition ratios (Olsen et al., 2013).  
94 Secondly, it's important to emphasize the absence of published documentation or feedback regarding the  
95 mechanical realization and the necessary operating procedures for obtaining measurements in line with theoretical  
96 performance for the SADS. It is well known that the details of mechanical design and manufacture have as much  
97 to do with impactor performance as the theoretical design: sealing, nozzle alignment (Loo and Cork, 1988),  
98 geometric assembly tolerances - these are all necessary qualities which are the consequence of a suitable  
99 mechanical design. So far, the SADS design proposed by Kim et al. has not been studied from these aspects, and  
100 it is possible that a more definitive version of the SADS will require a review of its overall mechanical design,  
101 without modification of the interior volume, which is perhaps optimal. Summarily, the authors who worked on the  
102 SADS have neither published documentation related to these aspects nor investigated them in previously published  
103 articles. In particular, it is doubtful whether the device as shown in Kim and Raynor (2010b) is leak-tight, with  
104 only two diametrically opposed clamping points. Also, in both versions, the proposed design does not seem to  
105 guarantee a precise control of nozzle spacing and alignment during assembly (limited guides and ground seats).  
106 Finally, it is not certain that the optimized version proposed in 2010 is really optimal for sampling semi-volatile  
107 aerosols encountered at workplaces, for various reasons. Firstly, from a methodological point of view, the  
108 optimization carried out is based on a Computational Fluid Dynamics (CFD) model, which does not appear to be  
109 sufficiently accomplished to provide enough accurate results for the optimization approach to have been  
110 conclusive, as exposed in Belut et al. (2022). This is notably illustrated by significant differences between CFD  
111 predictions and measurements, for both the airflow and the aerosol phase (modelled pressure drop on the major  
112 flow side is more than twice the measured value for Kim and Raynor (2009), measured and simulated particles  
113 separation efficiencies depart by as much as 30 % in Kim and Raynor (2009) and by as much as 53 % in Kim and  
114 Raynor (2010b), simulations report almost no particle deposition but experimental evaluations found important  
115 wall losses: 26.5 % for an aerosol with MMAD of 2.17  $\mu\text{m}$  in Kim and Raynor (2010a) and separate evaluations



116 by NIOH, Norway and Fraunhofer ITEM showed similarly high deposition ratios (Olsen et al., 2013). Secondly,  
117 the 2010 version has a much steeper inlet convergent angle (acceleration nozzle) than the 2009 version, which  
118 increases the probability of undesirable wall loss for the most inertial aerosols (Belut et al., 2022).

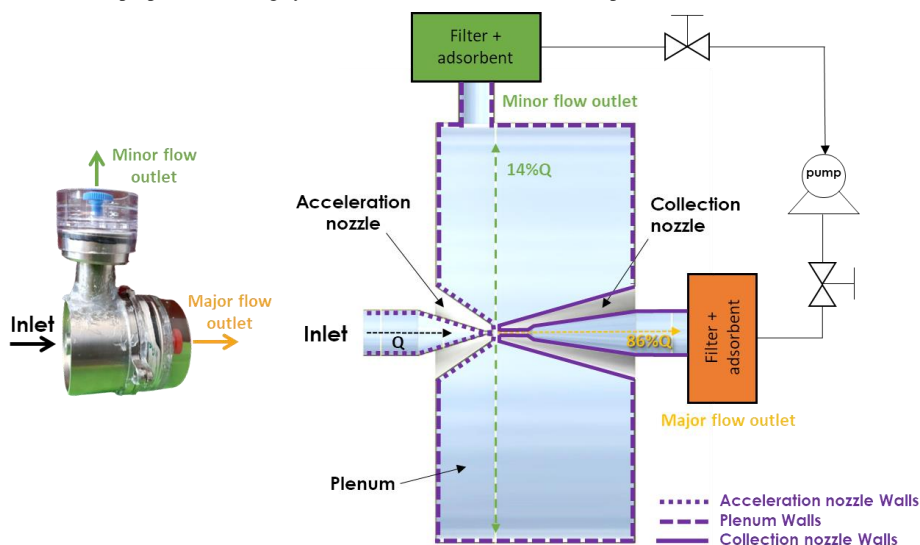
119 In this context, the present article proposes to:

- 120 - Investigate experimentally the size-resolved sampling performances of the SADS on liquid SVOCs  
121 particles in the range of aerodynamic diameter 0.15-4.5  $\mu\text{m}$ , i.e. beyond previous studies ;
- 122 - Identify practical issues related to the design, manufacturing and operation of the SADS such as proposed  
123 in Kim and Raynor (2009, 2010b) ;
- 124 - Investigate the effect of small variations of SADS nozzle diameters linked to inevitable random  
125 manufacturing uncertainties ;
- 126 - Detail the localization of wall losses in the device evoked in prior researches and identify their cause.

127 In doing so, our aim is to suggest improvement targets for future realization of the SADS, a small step to obtain a  
128 device suitable for the dichotomic measurement of particles and vapours composing SVOCs aerosols at  
129 workplaces. We shall base our study on the 2009 version of the SADS, because of the smaller cut-off diameter  
130 and also considering that the issues related to the overall design of the SADS are common to both versions.

131 To reach our objectives, five SADS prototypes were constructed and their sampling behaviour was characterized,  
132 using monodisperse liquid aerosols of various sizes. After evaluating the leakage resistance of the assembly, and  
133 its consequences on wall deposition, the actual sampling performances are compared to their theoretical  
134 counterparts computed by Belut et al. (2022). Origin of discrepancies are examined in terms of influence of the  
135 actually machined nozzle diameter and of the repeatability of the SADS assembly. An analysis of the distribution  
136 of deposits within the SADS is then used to estimate the likely cause of deposits in the device. The results are then  
137 discussed to propose improvement targets for the realization of the SADS, in terms of design and assembly.

138 Where necessary, CFD simulation results are used to support the observations. The approach of Belut et al. (2022)  
139 is then used for this purpose, including systematic calculation verification steps.



140

141 **Figure 1: Picture and schematic representation of a SADS prototype.**



## 142 2 Definitions and principle of particle-vapour dichotomous sampling

143 For a given aerodynamic diameter of particles  $d_a$ , the particles transmission efficiency  $\eta_p(d_a)$  to the particle  
144 major flow outlet is defined as the ratio of particle mass collected at the major flow outlet to the total particulate  
145 sampled mass of particles with the same diameter (Eq. 1):

$$146 \eta_p(d_a) = \frac{m_{major}(d_a)}{m_{inlet}(d_a)} \quad (1)$$

147 Similarly,  $\eta_v(d_a)$  is the particles transmission ratio to the particle minor flow outlet, defined by the ratio of the  
148 particle mass collected at the minor flow outlet to the total particulate sampled mass (Eq. 2), for a given particle  
149 size.

$$150 \eta_v(d_a) = \frac{m_{minor}(d_a)}{m_{inlet}(d_a)} \quad (2)$$

151 Finally, we defined a particles deposition ratio  $\eta_d(d_a)$  that correspond to the ratio of the mass deposited on the  
152 inner wall of the SADS to the total particulate sampled mass, for a given particle size (Eq. 3):

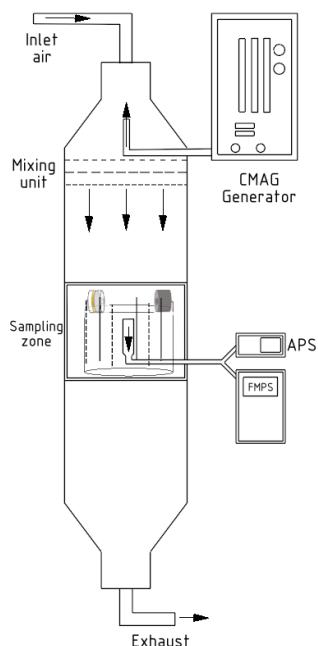
$$153 \eta_d(d_a) = \frac{m_{dep}(d_a)}{m_{inlet}(d_a)} \quad (3)$$

154 In ideal working conditions of the SADS as a gas-particle separator, we expect  $\eta_d$  to be zero while  $\eta_p=1$ . If this is  
155 verified, the particle and vapour concentration of SVOC in the sampled air can be easily obtained by collecting  
156 the total mass (vapour+particles) of SVOC at each outlet (minor and major) and by knowing that the minor outlet  
157 sample corresponds to vapours only (it is particle-free). The major outlet sample corresponds to particles and  
158 vapours, but the vapour contribution, known from the minor flow, can be subtracted to yield the particle  
159 concentration. However, this principle is valid only if  $\eta_d=0$  and  $\eta_p=1$  for the sampled aerosol size range, whence  
160 the necessity of finding the conditions under which this is valid in actual realization of the SADS.

## 161 3 Material and methods

### 162 3.1 Aerosol generation

163 To assess the performance of the Semivolatile Aerosol Dichotomous Sampler (SADS), aerosols were generated  
164 using a specialized equipment called the Bench for Organic Aerosol (BOA), as depicted in Figure 2. The BOA is  
165 a vertical wind tunnel designed to operate with controlled airflow velocities ranging from 0.1 to 0.5 m.s<sup>-1</sup> and  
166 humidity levels between 10 to 90 %RH. Aerosols were introduced countercurrent at the head of the tunnel to  
167 ensure thorough mixing with the airflow. To achieve spatially homogeneous mixtures at the sampling zone, the  
168 air/aerosol mixture passed through a series of diaphragms with different meshes. The SADS prototypes, along  
169 with an isokinetic nozzle connected to online instrument measurements, were placed on a crown support in the  
170 sampling zone.



171  
172

**Figure 2: Schematic drawing of the BOA generation device.**

173 To maintain consistent experimental conditions, room temperature was set to 21 °C, atmospheric pressure was  
174 measured at  $1018 \pm 10$  hPa, relative humidity was regulated at 20 %RH, and airflow velocity was fixed at  
175  $0.2 \text{ m}\cdot\text{s}^{-1}$ . The airflow inside the tunnel was considered isothermal, incompressible, and turbulent, with a Reynolds  
176 number based on the tunnel size of approximately  $4 \times 10^3$ .

177 The BOA was carefully calibrated to meet the requirements of the standard NF EN 13205-2:2014. Spatial  
178 homogeneity of velocities in the sampling section was confirmed, with the standard deviation below 1 % over the  
179 entire sampling zone. Similarly, the spatial homogeneity of particle concentration demonstrated standard deviation  
180 values below 10 %.

### 181 3.2 Aerosol generator

182 To produce aerosols for testing the SADS prototypes, a specialized Condensation Monodisperse Aerosol Generator  
183 (CMAG - TSI 3475) based on Sinclair-La Mer was employed. Originally designed for use with diethyhexyl  
184 sebacate (DEHS) and NaCl, the CMAG was modified to accommodate the use of glycerol and fluorescein. This  
185 modification was necessary as DEHS is not water-soluble, making the analysis of particles collected on filters or  
186 internal walls of the sampler challenging and less sensitive. By replacing DEHS with glycerol and NaCl with  
187 fluorescein, water-soluble droplets were generated, and fluorescein could be quantified at a very low concentration  
188 (i.e.,  $\text{LoQ} < 1 \text{ ng}\cdot\text{L}^{-1}$  within water extract).

189 The aerosol production process within the CMAG initiates with the nebulization of a water solution, specifically  
190 composed of  $0.8 \text{ g}\cdot\text{L}^{-1}$  fluorescein and  $5 \text{ g}\cdot\text{L}^{-1}$  sodium hydroxide in pure water, within an atomizer. This step is  
191 succeeded by the drying of the droplets in a diffusion dryer. Following the diffusion dryer, small nuclei, constituted  
192 of a blend of fluorescein and sodium hydroxide, were generated. These nuclei, serving as condensation nuclei,



193 exhibited sizes ranging from 10 to 100 nm. These nuclei were then exposed to a saturated vapour of glycerol  
194 downstream of the saturator. The resulting mixture of glycerol vapour and nuclei was directed to a re-heater and  
195 subsequently cooled down in a condensation chimney to produce the monodispersed aerosol.

196 It is important to note that the size of the generated particles could be adjusted by modifying the temperature of  
197 the saturator or the number concentration of nuclei. For this study, aerosols with mass median aerodynamic  
198 diameters (MMAD) of circa 0.15, 2, 3, and 4.5  $\mu\text{m}$  were produced and used for the experiments.

### 199 3.3 Aerosol characterization

200 Characteristics of the generated aerosols were measured continuously during the generation process. Aerodynamic  
201 particle sizes and geometric standard deviations (GSD) were measured using a TSI Aerodynamic Particle Sizer  
202 (APS 3321) associated with an aerosol diluter (TSI 3302 A) for particles ranging from 0.5 to 20  $\mu\text{m}$ . For particles  
203 ranging from 0.056 to 0.560  $\mu\text{m}$ , a TSI Fast Mobility Spectrometer (FMPS – 3091) was used. The FMPS apparatus  
204 measures a mobility diameter that was converted in this study in an aerodynamic diameter using the following  
205 equation:

$$206 \begin{aligned} d_m &= d_{ev} x \frac{Cu(d_m)}{Cu(d_{ev})}, \\ d_{ae} &= d_{ev} \left( \frac{Cu(d_{ev}) \rho_p}{Cu(d_{ae}) \rho_0 x} \right)^{1/2}. \end{aligned} \quad (4)$$

207 Where  $d_m$  the particle mobility diameter,  $d_{ae}$  the aerodynamic diameter,  $d_{ev}$  called the equivalent volume  
208 diameter:  $d_{ev} = \sqrt[3]{\frac{6V_p}{\pi}}$  with  $V_p$  the particles volume,  $Cu(d_m)$  the Cunningham slip correction factor based on  
209 electrical mobility diameter,  $Cu(d_{ev})$  The Cunningham slip correction factor based on aerodynamic diameter,  $\rho_p$   
210 particle density,  $\rho_0 = 1$  reference density, and  $x$  the shape factor (taken equal to 1 for the considered spherical  
211 particles).

212 The particle density exhibits variability between nuclei and condensed glycerol particles. Based on the initial  
213 composition of the fluorescein solution utilized for generating nuclei, the density of the nuclei was determined to  
214 be 1.72 after total desiccation. In contrast, the density of the condensed particles is approximated to the density of  
215 pure glycerol, given the negligible mass of the nuclei compared to the mass of glycerol that condenses on them.  
216 Consequently, particles with diameters of 2  $\mu\text{m}$  and above are considered to possess a density of approximately  
217 1.26.

218 To further enhance the relevance of this study, the physical diameter of the particles is approximated by the  
219 measured aerodynamic diameter, considering the spherical nature of the particles. This approximation facilitates  
220 the conversion of the number-based particle size distribution into a mass-based particle size distribution, a  
221 parameter of greater significance for our research objectives. Following the conversion from a number-based to a  
222 mass-based particle size distribution, we proceeded to calculate the mass median aerodynamic diameter (MMAD).  
223 This parameter serves as a valuable metric, providing a comprehensive characterization of the aerosol particles in  
224 our investigation.

225 The measurement of aerosol characteristic by APS and FMPS apparatus allow modulating the particle diameter  
226 produced by the CMAG and verifying the stability of the aerosol concentration during the experiment. Averages  
227 are shown in Table 1.

228 **Table 1: Averaged particle size distributions of the test aerosols (N=3  $\pm$  SD).**



Aerosol reference diameter ( $\mu\text{m}$ )	MMAD $\pm$ SD ( $\mu\text{m}$ )	GSD* $\pm$ SD
0.15	$0.16 \pm 0.05$	$1.56 \pm 0.02$
2	$2.04 \pm 0.15$	$1.16 \pm 0.03$
3	$3.17 \pm 0.21$	$1.14 \pm 0.01$
4.5	$4.70 \pm 0.12$	$1.10 \pm 0.02$

229 \*GSD: geometrical standard deviation.

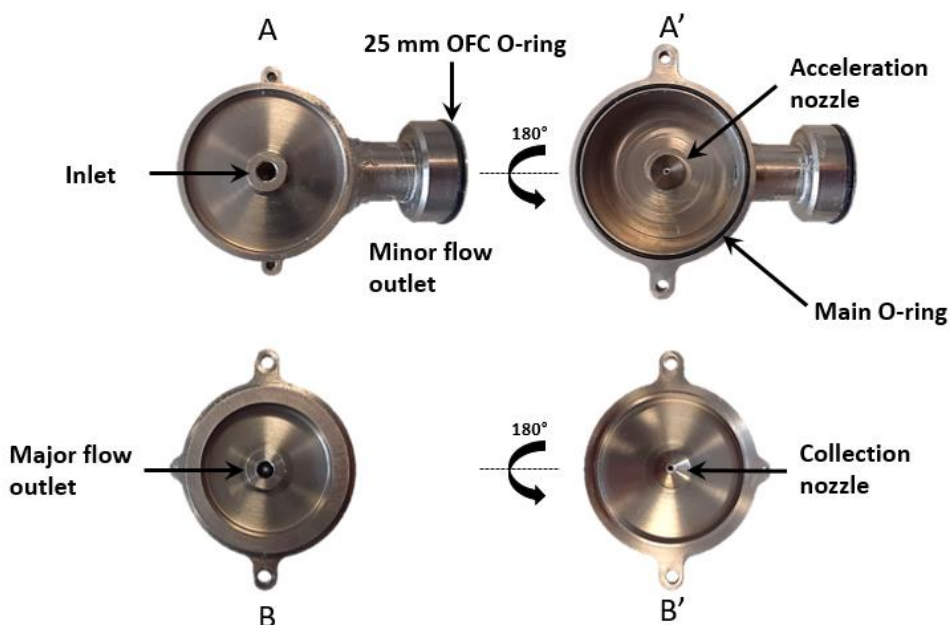
230 The stability of aerosol concentration in the sampling zone was verified, with a mass concentration deviation  
231 below 6 % across experiments.

### 232 3.4 SADS prototypes

233 The STAMI, Norway, had five titanium SADS Kim & Raynor (2009) prototypes manufactured by a precision  
234 mechanics workshop. Each prototype consisted of two main pieces: the acceleration part and the collection part,  
235 as shown in Figure 3. For all SADS prototypes, the actually machined nozzle diameters were measured using  
236 scanning electron microscopy (SEM). One of the manufactured SADS presented nozzle diameters exactly equal  
237 to those of the 2009 version of the SADS proposed by Kim & Raynor (2009): it was denoted SADS R and  
238 considered as the reference case for comparisons. The other SADS prototypes (SADS 1, SADS 2, SADS 3, and  
239 SADS 4) exhibited slight deviations in their nozzle diameters with respect to the SADS R, due to the inherent  
240 tolerance of the manufacturing process. The measured diameters of the acceleration and collection nozzles for  
241 each SADS prototype are presented in

242 Table 2. The maximum deviation of nozzle diameter with respect to the reference dimensions of SADS R (Kim  
243 and Raynor (2009) dimensions) was +0.03 mm (+3.7 %) for the acceleration nozzle and -0.05 mm (-4.5 %) for the  
244 collection nozzle.





245  
 246  
 247  
 248  
 249

**Figure 3:** Photographs of the SADS prototype, consisting of two main components - the acceleration nozzle (A') and the collection nozzle (B'). The upper left photo (A) shows the inlet side of the acceleration nozzle, while the lower left photo (B) displays the outlet side of the collection nozzle. On the outlet side of the collection nozzle (B), a 37 mm cassette is easily connected to the SADS sampler.

250  
 251

**Table 2: Nozzles diameters measured by SEM.**

SADS name	Acceleration nozzle [mm]	Collection nozzle [mm]	Ratio
	<i>(absolute difference with reference / relative difference with reference)</i>	<i>(absolute difference with reference / relative difference with reference)</i>	Collection nozzle / Acceleration nozzle
SADS 1	0.83 <i>(+0.03 / 3.7 %)</i>	1.05 <i>(-0.05 / -4.5 %)</i>	1.27
SADS 2	0.82 <i>(+0.02 / 2.5 %)</i>	1.06 <i>(-0.04 / -3.6 %)</i>	1.29
SADS 3	0.798 <i>(-0.002 / 0.3 %)</i>	1.11 <i>(+0.01 / + 0.9 %)</i>	1.39
SADS 4	0.818 <i>(+0.018 / 2.2 %)</i>	1.11 <i>(+0.01 / + 0.9 %)</i>	1.36
SADS R	0.8 <i>(+0.00 / 0 %)</i>	1.10 <i>(+0.00 / 0 %)</i>	1.38

252

### 3.5 Sampling procedure

253  
 254  
 255

The performance evaluation of the five SADS prototypes was conducted simultaneously in the sampling zone of the Bench for Organic Aerosol (BOA) (Figure 2). Prior to testing, each prototype was meticulously cleaned using ethanol and pure water. The samplers were equipped with Whatman Quartz Microfiber Filters (QMA) placed into



256 37 mm and 25 mm Open Face Cassettes (OFC) and connected at the major outlet and the minor outlet (Figure 1),  
257 respectively. The flow rates at the major flow outlet ( $1.8 \text{ L}\cdot\text{min}^{-1}$ ) and the minor flow outlet ( $0.3 \text{ L}\cdot\text{min}^{-1}$ ),  
258 corresponding to a total inlet flow rate of  $2.1 \text{ L}\cdot\text{min}^{-1}$ , were precisely controlled using flow meters (Gilian  
259 Gilibrator-2).

### 260 3.6 Fluorescence analysis

261 After each generation test, the sampling procedure for fluorescence analysis was carried out. The Whatman Quartz  
262 Microfiber Filters (QMA) contained in the 37 mm and 25 mm Open Face Cassettes (OFC) were extracted  
263 separately and analysed for fluorescence content. Each filter in the CFC and OFC was inserted into independent  
264 vials. A volume of 2 to 8 mL of the extraction solution, consisting of ultrapure water with a concentration of  $5 \text{ g}\cdot\text{L}^{-1}$   
265 of NaOH, was added to the vial to dissolve the collected droplets of glycerol and their fluorescein/sodium  
266 hydroxide nuclei. The walls of the CFC were also washed with the extraction solution (pure water basified with  
267  $5 \text{ g}\cdot\text{L}^{-1}$  of NaOH), and the resulting volume was combined with the one in the vial containing the CFC filter. After  
268 20 minutes of mechanical shaking, the extracts were filtered through a PTFE syringe filter with a pore size of about  
269  $0.2 \mu\text{m}$  to prevent any disruption of the fluorescence measurement.

270 Wall deposition inside the SADS was determined by using 2 mL of the extraction solution to wash each wall of  
271 the SADS separately. Three different extracts were obtained: one from the acceleration nozzle wall (carried particle  
272 mass  $m_{dep_a}$ ), one from the collection nozzle wall (carried particle mass  $m_{dep_c}$ ), and one from the plenum wall  
273 (carried particle mass  $m_{dep_p}$ ), (Figure 1).

274 The extracts were then analysed for fluorescence using a portable ESElog Fluorescence Detector (Qiagen,  
275 Germany), with an excitation wavelength of 485 nm and an emission wavelength of 520 nm. The linear range of  
276 the ESElog Fluorescence Detector defined the lower (LLOQ) and upper (ULOQ) limits of quantification, which  
277 covered the concentrations encountered in this work (LLOQ =  $0.33 \text{ ng}\cdot\text{L}^{-1}$ , ULOQ =  $4 \times 10^4 \text{ ng}\cdot\text{L}^{-1}$ ).

278 For each tested aerosol aerodynamic diameter  $d_a$ , the total sampled mass  $m_{inlet}$  is evaluated as the sum of sampled  
279 masses:

$$280 \quad m_{inlet} = m_{dep_a} + m_{dep_c} + m_{dep_p} + m_{major} + m_{minor}$$

281 and the fractional deposition ratio  $\eta_d(d_a)$  is computed as:

$$282 \quad \eta_d(d_a) = (m_{dep_a} + m_{dep_c} + m_{dep_p}) / m_{inlet},$$

283 and local deposition ratios at the acceleration nozzle ( $\eta_{d_a}$ ), collection nozzle ( $\eta_{d_c}$ ) and in the plenum ( $\eta_{d_p}$ ) are  
284 respectively computed from:  $\eta_{d_a} = m_{dep_a} / m_{inlet}$ ,  $\eta_{d_c} = m_{dep_c} / m_{inlet}$ ,  $\eta_{d_p} = m_{dep_p} / m_{inlet}$ , (so that  $\eta_d = \eta_{d_a} +$   
285  $\eta_{d_c} + \eta_{d_p}$ ).

286 Because monodispersed aerosols are used, the masses evoked in this paragraph are all linearly related to the amount  
287 of fluorescent dye that they carry. Hence, deposition ratios are directly computed from the measured masses of  
288 fluorescent dye.

### 289 3.7 Mass balance verification

290 A mass balance verification step was adopted to verify that the protocol allowed recovering all particles sampled  
291 by the SADS. The SADS prototypes and 37-mm Closed Face Cassettes (CFCs) were arranged alternately on the



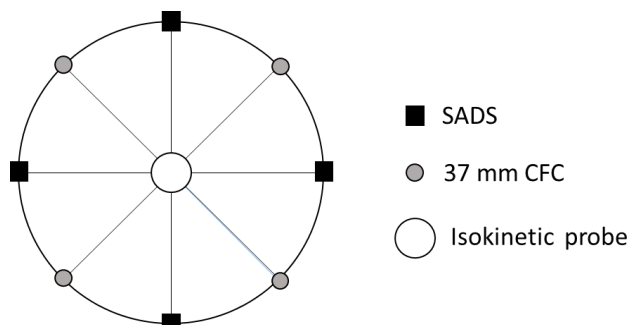
292 crown support (Figure 4). The 37-mm CFCs served as reference samplers, enabling the determination of the total  
293 mass of particles collected, in comparison to the particle mass measured by the SADS prototypes.  
294 All SADS and 37-mm CFCs presented a standardized 4 mm aerosol-sampling orifice and operated at the same  
295 sampling flow rate of 2.1 L.min<sup>-1</sup>. This standardization ensured that the total mass collected inside the 37-mm  
296 CFCs corresponded to  $m_{inlet}^i$ , the total mass sampled by the SADS, which includes the contribution of both the  
297 Open Face Cassettes (OFC) placed at the minor and major flow outlets and the wall deposits. By comparing  $m_{inlet}^i$ ,  
298 the total particle mass measured by the SADS  $i$ , with the mean reference mass measured by the 37-mm CFCs  
299 ( $\overline{m_{CFC}}$ ), we introduce the mass balance ratio of SADS  $i$  as:

$$300 \quad Mb_{SADS}^i = m_{inlet}^i / \overline{m_{CFC}} \quad (5)$$

301

302 This mass balance makes it possible to assess the overall efficiency of the protocol used to measure the distribution  
303 of particles collected by SADS, between deposits and major and minor outlets.

304 Additionally, the use of the 37-mm CFCs allows assessing the spatial homogeneity of the aerosol distribution  
305 within the sampling zone. No significant spatial variation was observed across different positions of the CFCs (CV  
306 < 5 %). With this assurance of spatial homogeneity, the individual SADS mass balance ( $Mb_{SADS}$ ) was calculated  
307 using equation 5 for each of the SADS prototypes.



308

309

Figure 4: Schematic representation of the positions of the samplers on the crown support.

310

### 3.8 Leak evaluation

311 Any form of leakage is known to compromise the sampling performances of aerosol samplers such as SADS, by  
312 disrupting the airflow and path lines within the nozzles and separation zone. Experimental tests were carried out  
313 to examine the leakage resistance of the proposed SADS assembly, to observe the effects of leaks and to determine  
314 an acceptable leakage limit for the SADS.

315 As the SADS operates under depression, a leakage test was performed using a digital pressure calibrator (DPC -  
316 FSM AG) set to a depression of -4000 Pa, equivalent to the operating pressure of the system. Following a  
317 stabilization period, the DPC's internal pump was deactivated, and the pressure was continuously measured to  
318 determine the leakage rate (LR) in Pa.s<sup>-1</sup> (Eq. 5). Three levels of leakage rates were defined: low, medium, and  
319 high, corresponding to LR values of  $LR \geq 13 \text{ Pa.s}^{-1}$ ,  $4 \text{ Pa.s}^{-1} \leq LR < 13 \text{ Pa.s}^{-1}$ , and  $LR < 4 \text{ Pa.s}^{-1}$ , respectively.

$$320 \quad LR = \frac{|P_0 - P_f|}{\Delta t} \quad (6)$$

321 Where  $P_0$  and  $P_f$  represent the pressures at  $t = 0$  s and at the final time, respectively, and  $\Delta t$  is the duration of the  
322 leak test.



### 323 **3.9 Supporting CFD Model**

324 The CFD modelling approach employed in this study to support observations is documented in detail in Belut et  
325 al. (2022). Simulations are conducted using ANSYS FLUENT V.19.3 software. After due examination of the most  
326 influent modelling and physical factors affecting the significance of results, a 2D axisymmetric reduction of the  
327 inner volume of the SADS is used to perform simulations. A low-Reynolds realizable k- $\epsilon$  turbulence model is used  
328 to model the incompressible airflow, with a free-inlet boundary condition at the entrance of the SADS, following  
329 the guidelines of Belut et al. (2022). Aerosol particle fates are computed through a Lagrangian tracking of their  
330 centre of mass, taking into account turbulent dispersion and using a free-inlet boundary condition at the inlet.  
331 External forces acting on particles are reduced to drag force, including rarefaction effect. Impaction and  
332 interception phenomena are taken into account for wall losses, particles being assumed trapped when hitting a wall  
333 (consistent with the liquid nature of present aerosols). An extensive verification of computations with respect to  
334 grid size, numerical resolution tolerances and number of used aerosol trajectories was performed, exactly as  
335 exposed in Belut et al. (2022). For further insights into the model's design and its applicability to the SADS,  
336 interested readers are encouraged to refer to the aforementioned study.

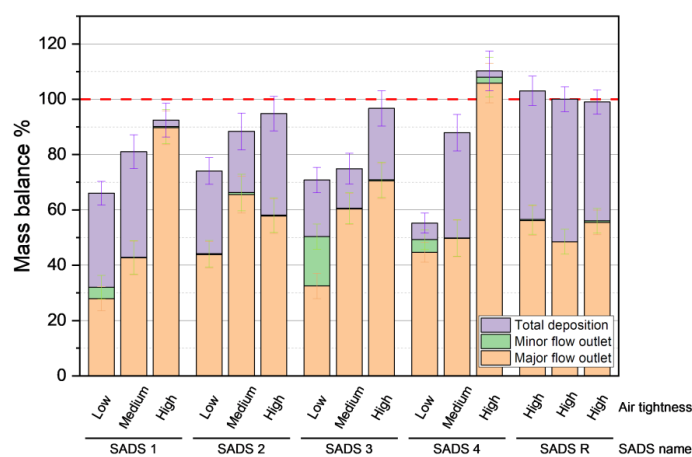
## 337 **4 Results and discussion**

### 338 **4.1 Leaks effects**

339 The airtightness tests conducted revealed significant leakages, primarily occurring at the O-ring seal between parts  
340 A and B (Figure 1) of the SADS prototypes. Additional leaks were also identified at the connection points between  
341 the Open Face Cassette (OFC) and the major and minor outlets of the SADS. Notably, SADS 1, 2, 3, and 4  
342 displayed varying levels of airtightness during the tests, with the exception of SADS R, which consistently  
343 exhibited high airtightness across all tests. Fig. 6 illustrates the evolution of mass balance and mass distributions  
344 for the five SADS prototypes with varying levels of air tightness.



345 The aerosol generated in the three tests was monodisperse with a size distribution centred on a MMAD of  
346  $3.11 \pm 0.21 \mu\text{m}$ , with a GSD of  $1.14 \pm 0.03$  and a particle number concentration of  $10124 \pm 320 \text{ pcl.cm}^{-3}$ .  
347 Tests on the leaks effects on the performance of the SADS were also conducted with aerosols having MMAD of  
348 2 and  $4.5 \mu\text{m}$ . The results and conclusions were consistent with the distributions presented, indicating that the  
349 outcomes converge towards those presented in the following section.



350

351 **Figure 5: Mass balance in the SADS prototypes in function of the airtightness level. Error bars represent the standard**  
352 **deviation calculated on five replicates for each condition.**

353 Low airtightness led to a substantial decrease in the mass balance of SADS 1, 2, 3, and 4 (Figure 5), with mass  
354 balances reaching  $66 \pm 6.2 \%$ ,  $74 \pm 6.8 \%$ ,  $70 \pm 6.58 \%$ , and  $55 \pm 7.59 \%$ , respectively. Only when a high level of  
355 airtightness was achieved could a mass balance of 90 % or higher be attained for all prototypes.

356 Moreover, low airtightness resulted in an undesirable increase in the mass fraction collected at the minor flow  
357 outlet. Presumably, leaks disturbed the airflow in the separation space, leading to the deviation of larger particles  
358 to the minor flow outlet than theoretically expected.

359 Globally, leaks not only influenced the total amount of particles collected within the SADS but also affected the  
360 particles transmission ratio to the major and minor outlets, which make results from leaky SADS unreliable.

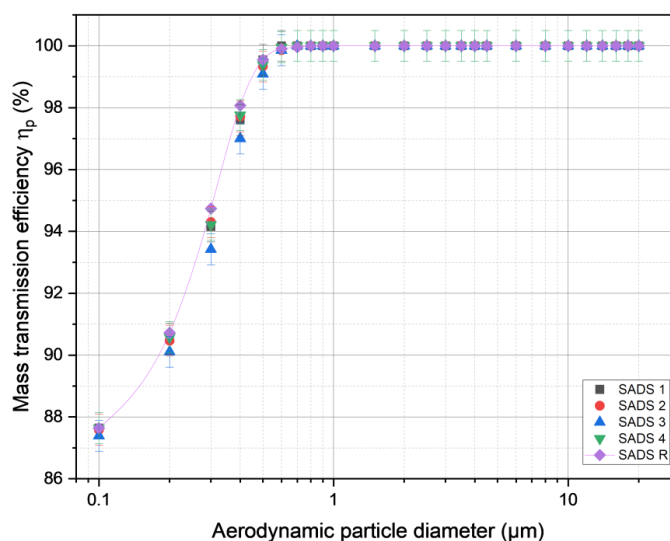
361 A systematic leak test is then mandatory before using the SADS for sampling purposes. To ensure reliable and  
362 accurate results, the SADS should only be considered suitable for sampling when the leakage rate ( $LR$ ) is below 4  
363  $\text{Pa}\cdot\text{s}^{-1}$ . Keeping the leakage rate within this acceptable limit will help maintain the integrity of the SADS and  
364 improve the reliability of the data collected during sampling operations. For further development, we also  
365 recommend revising the design of future realization of the SADS to guarantee its airtightness.

366 Due to difficulties in maintaining a constant level of airtightness for SADS 3 and 4 throughout all experimental  
367 tests, further experimentation with these two prototypes was not conducted.



368 **4.2 Theoretical effect of actually manufactured nozzle diameters**

369 Before comparing theoretical and actual performances of manufactured SADS, the effect of the lack of precision  
370 on the actually manufactured nozzle diameters is examined from a theoretical point of view, using the CFD model  
371 with the measured nozzle diameters of SADS 1, 2, 3, 4 and R. The numerical model computed the  $\eta_p$  curves for  
372 each SADS prototype across a range of aerodynamic particle diameters from 0.1 to 20  $\mu\text{m}$ , and the results are  
373 presented in Figure 6. Error bars correspond to one standard deviation of values arising from turbulent dispersion.



374

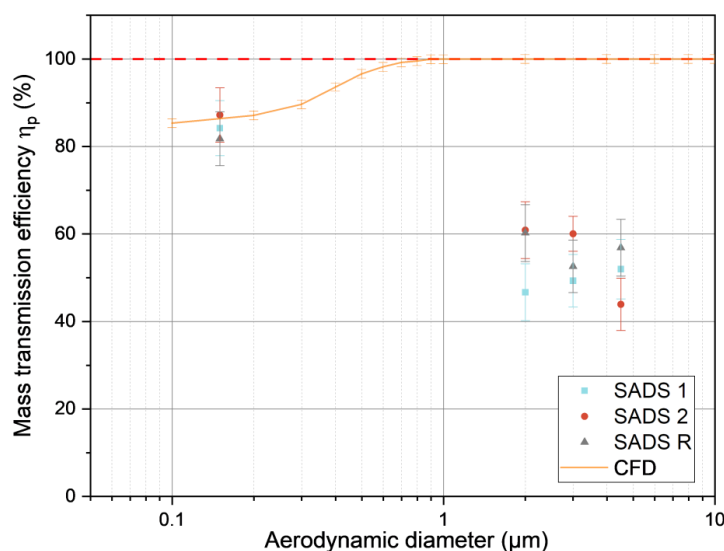
375 Figure 6: Evolution of CFD mass transmission of the SADS prototypes, accounting for variation in nozzle  
376 diameters.

377 The theoretical  $\eta_p$  curves calculated by the numerical model are similar for all SADS prototypes (Figure 6).  
378 SADS 3 exhibits the maximum difference compared to the reference SADS R transmission efficiency curve, but  
379 this difference remains below 3 % for all diameters. Overall, the variations observed in the nozzle diameters  
380 actually machined are not expected to lead to radically different sampling performance between the different  
381 prototypes.

382 These results are consistent with findings from a previous study on a VI by Marple & Chien, 1980a, who observed  
383 that increased ratios between nozzle diameters led to increased wall deposition, above the recommended value of  
384 1.33 (and thus to decreased transmission ratios). From Table 2, we indeed see that SADS 3 exhibits the largest  
385 nozzle diameters ratio (1.39) of the prototypes. All ratios are, however, in the 1.33-1.49 range recommended by  
386 Marple & Chien, 1980a.

387 **4.3 Actual vs. theoretical particle transmission efficiency**

388 Figure 7 compares the theoretical and actually measured  $\eta_p$  curves of the 3 airtight SADS.



389

390 **Figure 7: Comparison of theoretical CFD transmission efficiency  $\eta_p$  (SADS R) with experimental results for SADS 1,**  
391 **SADS 2, and SADS R. Error bars represent one standard deviation for CFD simulations due to turbulent dispersion**  
392 **and measuring uncertainty for experimental data.**

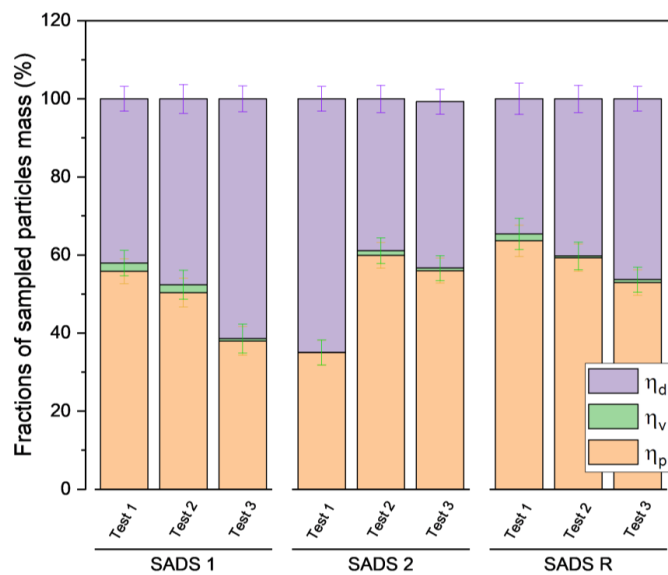
393 For aerosols with a reference diameter of 0.15  $\mu\text{m}$ , numerical predictions are in accordance with experimental  
394 tests, with transmission efficiencies to the major and minor flow outlets close to the ratio between the major and  
395 the minor flow ( $\eta_p = 86 \pm 0.58\%$  for the model and  $\eta_p = 81.7 \pm 6\%$  experimentally). This corresponds to the  
396 expected behaviour of non-inertial particles that are not separated by the SADS. We shall see, however, in the  
397 following section that a substantial fraction of these particles is actually deposited experimentally, in contradiction  
398 with theoretical results.

399 For the inertial particles tested with nominal diameters 2, 3 and 4.5  $\mu\text{m}$ ,  $\eta_p$  is measured as always less than about  
400 60 %, whereas 100 % is theoretically expected for the SADS in free-sampling situation. The origin of this  
401 difference is examined first by considering the particles deposition ratio in the next sections.

#### 402 4.4 Fate of inertial particles and repeatability issues

403 To illustrate the origin of the unexpectedly low transmission efficiency of inertial particles in the device, the  
404 distribution of all measured  $\eta_p$ ,  $\eta_v$  and  $\eta_d$  for 3 repetitions of the experiment and for the 3 airtight prototypes is  
405 shown on Figure 8 and Table 3. Only results for the 4.5  $\mu\text{m}$  particles are shown here for brevity. For these particles,  
406 we observe that the low transmission efficiency  $\eta_p$  is attributable to large ( $46.6 \pm 5.4\%$ ) wall losses ( $\eta_d$ ), and not  
407 to the misdirection of particles to the minor outlet. These deposits are not theoretically explained, even if we take  
408 into account the lack of precision of machined nozzle diameters (Figure 7), and we can note that they apparently  
409 vary randomly across repetitions with a large coefficient of variation for  $\eta_d$  (22.1 %). These variations are then  
410 likely to be attributable to the assembly process of the SADS, since other influencing parameters were monitored  
411 and controlled (flow rates, aerosol particle sizes, homogeneity of concentrations in the BAO, SADS leakage rate  
412 similarity of sampled masses).

413



414

415 **Figure 8: Distribution of the fate of inertial particles with a reference diameter of 4.5 μm in multiple repetitions, for**  
 416 **SADS 1, SADS 2, and SADS R at High Airtightness Level. Error bars represent the measuring uncertainty associated**  
 417 **with the data points."**

418

**Table 3: Transmission ratio to the major and minor outlets and deposition ratio for SADS 1, 2 and R.**

SADS name	Tests	$\eta_p$ [%]	$\eta_v$ [%]	$\eta_d$ [%]
SADS 1	Test 1	55.9	2.08	42.1
	Test 2	50.3	2.04	47.6
	Test 3	38.0	1.26	61.4
	Average	48.1	1.79	50.4
	SD	9.2	0.46	10.0
SADS 2	Test 1	35.0	0.07	64.9
	Test 2	59.9	1.26	38.9
	Test 3	56.0	0.64	43.4
	Average	50.3	0.66	49.0
	SD	13.4	0.60	13.9
SADS R	Test 1	63.6	1.73	34.6
	Test 2	59.3	0.48	40.2
	Test 3	53.0	0.75	46.3
	Average	58.6	0.99	40.4
	SD	5.4	0.66	5.8
Total Average		52.3	1.15	46.6
SD		5.6	0.58	5.4

419

#### 4.5 Detailed particles fate measured for SADS-R

420

Figure 9(a) and Figure 9(b) present images depicting a typical deposition that occurs inside the SADS after the sampling process. Notably, a significant amount of liquid particles can be seen on the external walls of the nozzles.

421

Deposits can also be found on the internal walls of the nozzles, but they are difficult to capture in photographs.

422





423 Additionally, in certain tests, projections of macroscopic droplets from the nozzles to the walls of the plenum were  
 424 also observed.



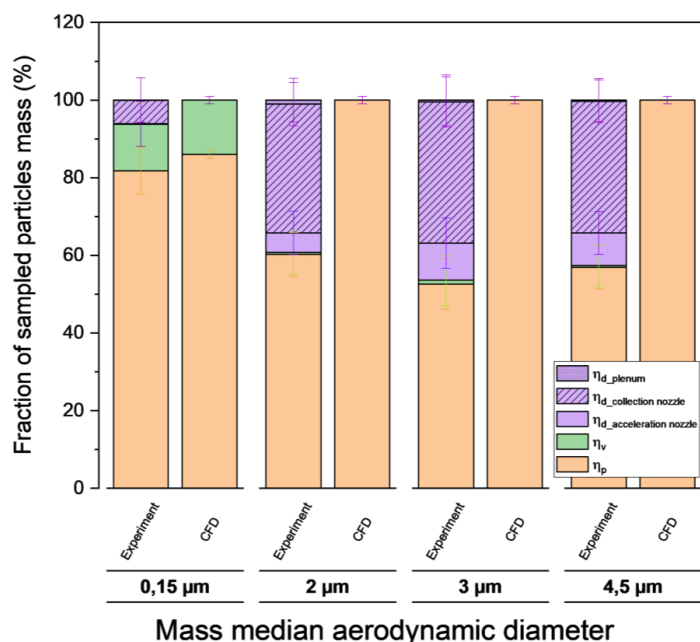
(a) acceleration nozzle (b) Collection nozzle

**Figure 9: Pictures of particles deposition outside the nozzle.**

428 To better understand the localization and underlying reasons for particle deposition in the SADS, independently  
 429 of variations between prototypes, the detailed transmission ratios and position-resolved deposition ratios for the  
 430 reference SADS-R are given on Figure 10, for all tested particle sizes. Values are averaged over 3 repetitions.

431 For particles with reference diameter  $0.15 \mu\text{m}$ , wall deposition is primarily located on the collection nozzle, with  
 432  $6 \pm 5.8 \%$  of sampled mass, though it should be almost zero theoretically ( $0.44 \pm 0.58 \%$ ).

433 For particles with reference diameters  $2, 3$  and  $4.5 \mu\text{m}$ , the experimental results show substantial particle  
 434 depositions ( $43 \%$  of sampled mass in average), unpredicted by theory either ( $0.2 \pm 0.1 \%$ ). These experimental  
 435 wall deposits seem almost independent of particle diameter for these inertial particles. The distribution of deposits  
 436 across zones reveals that the majority of particles deposit on the collection nozzle ( $34.5 \pm 3.4 \%$ ), followed by the  
 437 acceleration nozzle ( $7.6 \pm 3.4 \%$ ), with minimal deposition in the plenum ( $0.6 \pm 3.4 \%$ ).



438

439 **Figure 10: Mass distribution in SADS R exposed to four different particle size distributions: experimental and**  
 440 **numerical study for precise wall deposition localization and transmission efficiency analysis. (Three repetitions, error**  
 441 **bars represent measuring uncertainty). It is essential to note that most of the deposits observed can contaminate the**  
 442 **vapour phase measurements at the minor outlet if particles evaporate after deposition. Indeed, wall deposition on the**



443 **acceleration nozzle is located before separation, and most of the deposit of the collection nozzle is actually located on its**  
444 **outside walls (fraction of the deposit which is visible to the unaided eye).**

445 Having ruled out the effects of leakage and machining inaccuracies in nozzle diameter, we can envisage several  
446 reasons for these deposits, which are not predicted by the numerical model. Firstly, the simulated geometry may  
447 not correspond to the real geometry for aspects other than nozzle diameter. In particular, the variations in deposits  
448 between the tests (Figure 8 and Figure 10) suggest variability in the assembly of the 2 parts of the SADS in relation  
449 to each other, and therefore a geometry of the interior domain of the SADS that is not only variable but also  
450 different from what is simulated. These variations may correspond in particular to a misalignment of the nozzles  
451 with respect to each other, which can easily explain the impaction of inertial particles outside the collection nozzle  
452 (Loo & Cork, 1988). In the following section, the sensitivity of SADS performances with respect to nozzle  
453 misalignment is thus illustrated theoretically.

#### 454 **4.6 Theoretical effect of nozzle misalignment**

455 Study by Loo & Cork (1988) emphasized the importance of maintaining axial misalignment between the  
456 acceleration and collection nozzle of a VI. In their case, which is very different from the SADS in terms of  
457 dimensions and air flow rates, they recommend avoiding an offset of more than 1.6 % of nozzle diameter and  
458 observe that each 1.6 % increase in misalignment leads to a 1 % increase in nozzle wall loss. Meeting this criterion  
459 in the case of the SADS would mean avoiding a misalignment of more than 0.013 mm, which is challenging from  
460 a mechanical design point of view. Experimentally, measuring the misalignment offset of the mounted SADS was  
461 not feasible. However, a sensitivity analysis can be performed by means of parametric CFD computations to  
462 explore the impact of this parameter.

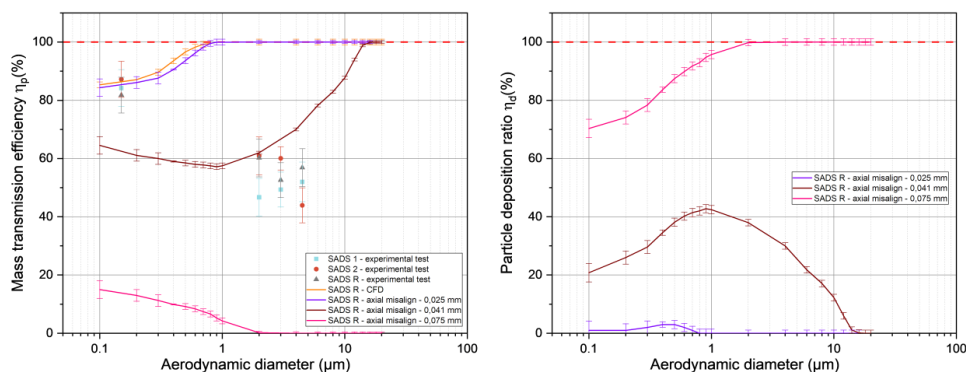
463

464 Simulations were hence carried out with relative displacements of the collection nozzle with respect to the  
465 acceleration nozzle (Figure 1) in the Z-axis direction, with likely values of the axial backlash between the two  
466 parts of the SADS. These parts are assembled by manually fitting together a shaft and a 37 mm diameter hole.  
467 Following ISO system of limits and fits, this corresponds to a H7/h6 clearance fit (location fit), whence a possible  
468 axial backlash in the range 0 to 0.041 mm is deduced. Parametric computations were then performed for axial  
469 backlashes of 0, 0.025 and 0.041 mm respectively (corresponding to 0, 3.1 % and 5.1 % of the nozzle diameter  
470 respectively). A simulation with an extreme backlash of 0.075 mm (9.4 % of nozzle diameter) was also performed  
471 for information, which could correspond to a more tolerant H8/f7 ISO clearance fit (close-running fit).

472 Figure 11 displays the corresponding numerical simulation results for the transmission efficiency and wall  
473 deposition, compared with experimental measurements of SADS 1, 2, and R, illustrating the possible effect of  
474 axial misalignment on  $\eta_p$ .



475



476

477

**Figure 11: Numerical simulations results of misalignment effect compared with experimental tests**

478

Results show that likely values of the axial mechanical backlash between the two parts lead to a severe decrease of  $\eta_p$  due to dramatically increasing wall losses  $\eta_d$  on the collection nozzle external walls, especially for the most inertial particles. This finding is compatible with experimental measurements. Axial misalignment of the device is therefore a possible cause of the differences in performance between the ideal version and the mechanical realization of the SADS, for the most inertial particles tested. Of course, present simulations can only qualitatively reproduce the tendency of the experiment, since they were not performed with the actual axial backlash which is unknown and which varies between each SADS assembly. Also, the effects of other existing mechanical backlashes were not numerically tested and necessarily contribute to sampling performances (tolerance on the separation length between nozzles, existing angle between the axes of the two parts of the SADS, etc.).

487

Based on the analysis of the results, we can conclude that the maximum allowable misalignment during the assembly of the SADS, between the collection nozzle and the acceleration nozzle, is established at 0.025 mm, as evidenced by the violet curve. Notably, this curve consistently aligns with that of the SADS R-CFD, representing a curve with perfect alignment.

490

## 491 5 Conclusion and discussion

492

This study experimentally evaluated the dichotomous sampling performance (gas and particles) of 5 SADS prototypes of identical design, and for an aerosol of liquid particles with aerodynamic diameters of 0.15, 2, 3 and 4.5  $\mu\text{m}$ .

494

495

Lab tests were carried out in a dedicated controlled generation environment, the BAO, in which monodisperse aerosols marked with a fluorescent dye were emitted, thanks to the modification of the CMAG generator to accommodate the use of glycerol and fluorescein as condensing vapour and nuclei respectively.

497

498

SADS sampling performance in terms of total mass sampled, particle fraction transmitted to the major outlet and particle losses at the walls were put into perspective with the details of mechanical construction and with the operating conditions of the prototypes: leak rate, repeatability between successive assemblies, imprecision of machined nozzles diameters, and axial misalignment of the assembly.

501



502 The measured sampling performances were compared to their theoretical counterparts computed by CFD in Belut  
503 et al. (2022), and CFD was also used to study the theoretical effect of variations in the geometry of machined  
504 SADS relative to the plans, regarding the nozzles diameters and nozzle misalignments.  
505 With the originally proposed design, the SADS assembly was found easily leaky, but consequences on sampling  
506 could be overcome when a prior leak test with leakage rate LR below  $4 \text{ Pa}\cdot\text{s}^{-1}$  was passed.  
507 Sampling performances were found little reproducible during successive SADS assemblies (between tests,  
508  $\text{CV}=22.1 \%$  for wall losses). Theoretically unpredicted large (40-46 % of sampled mass) wall losses were  
509 measured for particles larger than  $2 \mu\text{m}$ , located mostly (80 %) on the external walls of the collection nozzle.  
510 Assembly repeatability issues and simulations of SADS parts misalignment effect by CFD suggest that these  
511 undesirable particle deposits are due to the mechanical backlashes of the assembly, and not to the imprecision of  
512 actually machined nozzles diameters. Indeed, the measured variation of nozzle diameters in the range ( $-4.5 \%$ ,  
513  $+3.7 \%$ ) with respect to nominal values were found to theoretically affect marginally ( $<3 \%$ ) aerosol transmission  
514 efficiencies.  
515 Present results suggest that although the dichotomous sampling performances of the SADS are theoretically  
516 interesting for workplace exposure assessment to SVOC aerosols, its actual realization fails in reaching theoretical  
517 performances for micron-sized particles, due to mechanical design issues. Airtightness, nozzle alignment and  
518 repeatability of assembly are not sufficiently guaranteed by its initial design and future development should focus  
519 on improving these aspects to obtain a sampler suitable for field studies.  
520 However, several biases may have affected the findings of the study. For example, rare macroscopic particles are  
521 sometimes emitted by the CMAG and may have been sampled by the SADS, biasing the separation performance  
522 measurements and especially the deposition measurements. However, we believe that this possibility is largely  
523 controlled by the real-time monitoring of particle sizes in the test rig, and by the simultaneous use of several SADS  
524 in the test rig. Regarding the plausibility of the simulation results, it is, of course, limited by the physical  
525 phenomena actually taken into account. Calculation errors are limited by the verification procedure used (Belut et  
526 al., 2022), which guarantees a numerical error of less than  $0.5 \%$  on the particulate fractions deposited and  
527 transmitted. However, actual variations in the geometry of assembled SADS compared with the drawings (due to  
528 machining inaccuracies other than nozzle diameters) are not taken into account, nor is wall roughness, despite its  
529 acknowledged effect on deposits. The roughness of the machined acceleration nozzles could therefore help to  
530 explain the deposition of particles in this nozzle, which are not predicted by calculations that assume a perfectly  
531 smooth nozzle. Similarly, the more or less pronounced sharpness of the sampling orifice actually machined can  
532 have a significant influence on the inlet particle velocity and concentration profile, and therefore on the actual  
533 performance of the SADS (Belut et al., 2022).  
534 Nevertheless, the lack of repeatability of SADS performance between successive assemblies, its low and variable  
535 airtightness level and its radial clearance large enough to cause a significant misalignment of the nozzles (typically  
536  $5 \%$ ) have sufficiently important effects for these possible limitations of the study not to call into question its  
537 conclusions.  
538 By addressing the identified challenges and incorporating further refinements in the SADS design and operation,  
539 researchers can enhance its reliability, accuracy, and applicability in various aerosol sampling applications,  
540 contributing to advancements in aerosol science and related fields.



541 **7 Table of Symbols**

$\eta_p$	particles transmission efficiency to the particle outlet (major flow)	
$\eta_v$	particles transmission efficiency to the vapour outlet (minor flow)	
$\eta_d$	particles deposition ratio	
$\eta_{d_a}, \eta_{d_c}, \eta_{d_p}$	particles deposition ratio in the acceleration nozzle, collection nozzle and in the plenum respectively	
$m_{major}$	Mass of particles collected at the major flow outlet	(ng)
$m_{minor}$	Mass of particles collected at the minor flow outlet	(ng)
$m_{inlet}$	Mass of sampled particles at the inlet	(ng)
$m_{dep}$	Mass of deposited particles	(ng)
MMAD	Mass median aerodynamic diameter	
GSD	Geometric standard deviation	
LR	Leakage rate	(Pa.s <sup>-1</sup> )
T	Temperature	(°C)
P	Pressure	(Pa)
$Mb_{SADS}$	Mass balance of SADS	
$m_{CFC}$	Mass measured by the closed face cassettes	(ng)
LLOQ	Lower limit of quantification	ng.L <sup>-1</sup>
ULOQ	Upper limit of quantification	ng.L <sup>-1</sup>
WD	Wall depositions	
$m_{WL}$	Quantity of fluorescein measured in the wall	ng
$m_{tot}$	Total quantity of fluorescein sampled by the SADS	
$U_i$	Air velocity	m.s <sup>-1</sup>
$\rho$	Air density	Kg.m <sup>3</sup>
$\mu$	Air viscosity	Pa.s <sup>-1</sup>

542 **8. Author contribution**

543 BS, EB, EG and RO conceptualized the research project. NR, BS and EB developed the methodology and NR was  
 544 responsible of the investigation. BS and EB validated the results. EG was responsible for the supervision of the  
 545 project. NR wrote the original draft preparation and BS, EB and EG reviewed and edited the manuscript.

546 **9. Competing interests**

547 The authors declare that they have no conflict of interest.



548 **10. Financial support**

549 This research did not receive any specific grant from funding agencies in the public, commercial, or not-for-profit  
550 sectors.

551 **8 Bibliography**

552 Belut, E., Rekeb, N., Sutter, B., and Géhin, E.: Revisiting the CFD modeling of a virtual impactor with inverted  
553 split ratio: Highlighting some determinants of representativeness, *J. Aerosol Sci.*, 166, 106068,  
554 <https://doi.org/10.1016/j.jaerosci.2022.106068>, 2022.

555 Cooper, S. J., Raynor, P. C., and Leith, D.: Evaporation of Mineral Oil in a Mist Collector, *Appl. Occup. Environ.*  
556 *Hyg.*, 11, 1204–1211, <https://doi.org/10.1080/1047322X.1996.10389398>, 1996.

557 Kim, S. W. and Raynor, P. C.: A New Semivolatile Aerosol Dichotomous Sampler, *Ann. Occup. Hyg.*, 53, 239–  
558 248, <https://doi.org/10.1093/annhyg/mep008>, 2009.

559 Kim, S. W. and Raynor, P. C.: Experimental Evaluation of Oil Mists Using a Semivolatile Aerosol Dichotomous  
560 Sampler, *J. Occup. Environ. Hyg.*, 7, 203–215, <https://doi.org/10.1080/15459620903582244>, 2010a.

561 Kim, S. W. and Raynor, P. C.: Optimization of the Design of a Semivolatile Aerosol Dichotomous Sampler,  
562 *Aerosol Sci. Technol.*, 44, 129–140, <https://doi.org/10.1080/02786820903426739>, 2010b.

563 Kim, S. W., Lee, E. G., Lee, T., Lee, L. A., and Harper, M.: Exposure to chlorpyrifos in gaseous and particulate  
564 form in greenhouses: a pilot study, *J. Occup. Environ. Hyg.*, 11, 547–555, 2014.

565 Leith, D., Leith, F. A., and Boundy, M. G.: Laboratory Measurements of Oil Mist Concentrations Using Filters  
566 and an Electrostatic Precipitator, *Am. Ind. Hyg. Assoc. J.*, <https://doi.org/10.1080/15428119691014242>, 2010.

567 Lillienberg, L., Burdorf, A., Mathiasson, L., and Thörneby, L.: Exposure to Metalworking Fluid Aerosols and  
568 Determinants of Exposure, *Ann. Occup. Hyg.*, 52, 597–605, <https://doi.org/10.1093/annhyg/men043>, 2008.

569 Loo, B. W. and Cork, C. P.: Development of High Efficiency Virtual Impactors, *Aerosol Sci. Technol.*, 9, 167–  
570 176, <https://doi.org/10.1080/02786828808959205>, 1988.

571 Marple, V. A. and Chien, C. M.: Virtual Impactors: A Theoretical Study, *Environ. Sci. Technol.*, 14, 976–985,  
572 <https://doi.org/10.1021/es60168a019>, 1980.

573 Olsen, R., Thomassen, Y., Koch, W., Halgard, K., Bakke, B., and Ellingsen, D. G.: Performance testing of a  
574 personal sampler for full-shift sampling of oil mist and oil vapour, STAMI National Institute of Occupational  
575 Health, 2013.

576 Park, D., Stewart, P. a, and Coble, J. B.: Determinants of Exposure to Metalworking Fluid Aerosols: A Literature  
577 Review and Analysis of Reported Measurements, *Ann. Occup. Hyg.*, 53, 271–288,  
578 <https://doi.org/10.1093/annhyg/mep005>, 2009.

579 Park, S. S., Kang, M. S., and Hwang, J.: Oil mist collection and oil mist-to-gas conversion via dielectric barrier  
580 discharge at atmospheric pressure, *Sep. Purif. Technol.*, 151, 324–331,  
581 <https://doi.org/10.1016/j.seppur.2015.07.059>, 2015.

582 Raffy, G., Mercier, F., Gloennec, P., Mandin, C., and Le Bot, B.: Oral bioaccessibility of semi-volatile organic  
583 compounds (SVOCs) in settled dust: A review of measurement methods, data and influencing factors, *J. Hazard.*  
584 *Mater.*, 352, 215–227, <https://doi.org/10.1016/j.jhazmat.2018.03.035>, 2018.

585 Raynor, P. C. and Leith, D.: Evaporation of accumulated multicomponent liquids from fibrous filters, *Ann. Occup.*  
586 *Hyg.*, 43, 181–192, <https://doi.org/10.1093/annhyg/43.3.181>, 1999.



- 587 Raynor, P. C., Volckens, J., and Leith, D.: Modeling Evaporative Loss of Oil Mist Collected by Sampling Filters,  
588 Appl. Occup. Environ. Hyg., 15, 90–96, <https://doi.org/10.1080/104732200301890>, 2000.
- 589 Roberts, J. W., Wallace, L. A., Camann, D. E., Dickey, P., Gilbert, S. G., Lewis, R. G., and Takaro, T. K.:  
590 Monitoring and Reducing Exposure of Infants to Pollutants in House Dust, in: Reviews of Environmental  
591 Contamination and Toxicology Vol 201, edited by: Whitacre, D. M., Springer US, Boston, MA, 1–39, 2009.
- 592 Simpson, A. T.: Comparison of Methods for the Measurement of Mist and Vapor from Light Mineral Oil–Based  
593 Metalworking Fluids, Appl. Occup. Environ. Hyg., 18, 865–876, <https://doi.org/10.1080/10473220390237386>,  
594 2003.
- 595 Simpson, A. T., Groves, J. A., Unwin, J., and Piney, M.: Mineral oil metal working fluids (MWFs)—development  
596 of practical criteria for mist sampling, Ann. Occup. Hyg., 44, 165–172, <https://doi.org/10.1093/annhyg/44.3.165>,  
597 2000.
- 598 Sutter, B., Bémer, D., Appert-Collin, J.-C., Thomas, D., and Midoux, N.: Evaporation of Liquid Semi-Volatile  
599 Aerosols Collected on Fibrous Filters, Aerosol Sci. Technol., 44, 395–404,  
600 <https://doi.org/10.1080/02786821003674244>, 2010.
- 601 Technical Overview of Volatile Organic Compounds: [https://www.epa.gov/indoor-air-quality-iaq/technical-](https://www.epa.gov/indoor-air-quality-iaq/technical-overview-volatile-organic-compounds)  
602 [overview-volatile-organic-compounds](https://www.epa.gov/indoor-air-quality-iaq/technical-overview-volatile-organic-compounds), last access: 5 February 2020.
- 603 Volckens, J.: Partitioning Theory for Respiratory Deposition of Semivolatile Aerosols, Ann. Occup. Hyg., 47,  
604 157–164, <https://doi.org/10.1093/annhyg/meg015>, 2003.
- 605 Volckens, J., Boundy, M., Leith, D., and Hands, D.: Oil Mist Concentration: A Comparison of Sampling Methods,  
606 Am. Ind. Hyg. Assoc. J., <https://doi.org/10.1080/00028899908984492>, 2010.
- 607 Wlaschitz, P. and Höflinger, W.: A new measuring method to detect the emissions of metal working fluid mist, J.  
608 Hazard. Mater., 144, 736–741, <https://doi.org/10.1016/j.jhazmat.2007.01.104>, 2007.
- 609